Transport properties and flux pinning by self-organization in $YBa_2Cu_3O_{7-\delta}$ films on vicinal $SrTiO_3(001)$

T. Haage, J. Zegenhagen, J. Q. Li, H.-U. Habermeier, and M. Cardona
Max-Planck-Institut für Festkörperforschung, Heisenbergstrasse 1, D-70569 Stuttgart, Federal Republic of Germany

Ch. Jooss, R. Warthmann, A. Forkl, and H. Kronmüller
Max-Planck-Institut für Metallforschung, Heisenbergstrasse 1, D-70569 Stuttgart, Federal Republic of Germany
(Received 13 May 1997)

We have observed anisotropic flux pinning and resistivity in the substrate plane of $YBa_2Cu_3O_{7-\delta}$ (YBCO) thin films grown on vicinal $SrTiO_3(001)$ with the *c* axis oriented along the $SrTiO_3$ [001] direction. Using UHV scanning tunneling microscopy and transmission electron microscopy we demonstrate the influence of a periodic nanoscale step structure of the clean substrate surface on the morphology and defect microstructure of subsequently deposited YBCO films. A linear array of dislocations generated via self-organization of the YBCO leads to an exceptionally large critical current density up to 8×10^{11}A/m^2 at 4.2 K. The findings indicate that the critical current density of high-temperature superconductors can be enhanced in a controlled way growing thin films on tailored substrate surfaces. [S0163-1829(97)07537-1]

I. INTRODUCTION

The nature of flux pinning in high-temperature superconductors (HTSC's) is of fundamental and technological interest. The polyatomic composition of HTSC's leads to a wide range of possible defects which may give rise to different pinning mechanisms with varying efficiency. To shed light on these issues, a systematic investigation of the interplay between different types of *intrinsic* defects and flux pinning is needed.

It has been found that randomly distributed point defects (i.e., oxygen vacancies) in $YBa_2Cu_3O_{7-\delta}$ (YBCO) single crystals lead to a weak collective pinning,[1,2] whereas twin boundaries cause a correlated pinning as well as a channeling of vortices along twin planes.[3] Moreover, *artificial* columnar defects fabricated by heavy-ion irradiation cause strong correlated pinning.[4] Specifically, crossed columnar defects enhance the critical current density j_c up to 1×10^{10} A/m^2 (4.2 K) in YBCO single crystals.[5]

It is well known that epitaxial YBCO thin films exhibit a critical-current density which is at least one order of magnitude larger than that of twinned single crystals. Grain boundaries,[6] precipitates,[7] intrinsic pinning,[8] surface roughness,[9] dislocation chains in growth terraces,[10] and screw dislocations[11] have been suggested as a possible source of effective pinning in YBCO films. But despite the enormous efforts, the strong pinning sites generated during film growth have not yet been identified.

However, the layered structure of HTSC's and thermal fluctuations resulting in a depinning of vortices, require coherent defects (i.e., line or planar defects) to achieve effective pinning and large j_c. For example, it has been found[12] that *columnar* defects in YBCO films which originate from a mosaicity of a 1.6° miscut $LaAlO_3$ substrate enhance j_c in an external magnetic field of 1 T, oriented between the *c* axis and the CuO_2 planes [$j_c(B=1$ T, 77 K) $= 0.52\times10^{10}$ A/m^2], while at zero magnetic field the critical current density [$j_c(B=0$, 77 K) $= 2.02\times10^{10}$ A/m^2] shows a magnitude commonly observed in epitaxial films. It has been recently suggested[13] on the basis of the temperature dependence of j_c that a spatial variation in the charge-carrier mean free path *l* near lattice defects leads to effective pinning in epitaxial $YBa_2Cu_3O_7$ and $YBa_2Cu_4O_8$ films. This mechanism is called δl pinning, in contrast to δT_c pinning,[1,14] where disorder causes a suppression of the superconducting order parameter associated with a spatial variation of the transition temperature T_c.

Here we demonstrate an unusual approach, the controlled generation of an array of antiphase boundaries with an extended, *planar* structure via self-organization of YBCO on vicinal $SrTiO_3(001)$ surfaces. Pinning by these coherent defects results in a substantial enhancement of $j_c(B=60$ mT, 4.2 K) up to 8×10^{11} A/m^2. Moreover, this set of coherent defects causes an anisotropy of the magnetic flux penetration in the *ab* plane when the weak external magnetic field is oriented parallel to the *c* axis (i.e., perpendicular to the CuO_2 planes and correspondingly parallel to the defect planes).

The large density of defects necessary to achieve effective pinning has significant impact on the transport properties of the epitaxial thin film: We observe a pronounced anisotropy of the in-plane resistivity, as well as a small reduction of T_c. However, the electronic conductivity in YBCO films on vicinal $SrTiO_3(001)$ substrates is a combination of in-plane and out-of-plane transport modified by defect scattering. Studying the systematics of the resistivity as a function of film thickness we can gain insight into the nature of charge transport in epitaxial thin films.

II. EXPERIMENTAL PROCEDURES

YBCO films with a thickness ranging from 24 to 360 nm were grown by pulsed laser deposition (PLD). The PLD chamber is coupled to a UHV system with a base pressure of about 5×10^{-11} mbar. This enables us to perform most of

our studies *in situ*. The $SrTiO_3(001)$ substrates were cut and polished 1.2° or 10° off the (001) plane toward [010] as confirmed by x-ray diffraction. The substrates were annealed in UHV ($\leqslant 10^{-9}$ mbar) at a temperature of 950 °C for 2 h. This sufficed to generate a well ordered and clean surface, as judged by low-energy electron diffraction (LEED) and Auger electron spectroscopy. The loss of oxygen during UHV annealing results in *n*-type conductivity which enables us to image the clean substrate surfaces by UHV-scanning tunneling microscopy (STM) prior to deposition. The YBCO films were grown at a substrate temperature of 750 °C in an oxygen pressure of 0.2 mbar, oxygenated (in 750 mbar O_2) immediately after deposition, and cooled to 450 °C. The samples were kept at this temperature for 20 min and finally cooled to room temperature. This procedure was optimized in terms of the superconducting properties (i.e., maximum transition temperature $T_c \approx 90$–91 K) of films with a thickness of more than 120 nm grown on well-oriented $SrTiO_3(001)$ substrates which exhibit atomically flat terraces, more than 250 nm wide, as revealed by UHV-STM.

After the PLD process the deposition chamber was pumped to a pressure of less than 10^{-7} mbar and the samples were transferred to the STM stage without exposing them to air. All STM images were taken in the constant current mode with tunneling currents of 0.2–0.3 nA and a positive sample bias of 0.75–1.9 V. Our STM achieves a resolution better than 0.01 nm (0.2 nm) vertically (laterally) on semiconductor surfaces. The STM scanner was calibrated with the 7×7 reconstruction of a Si(111) surface.

The quality of the epitaxy, i.e., the degree of twinning and growth-related strains in our YBCO films, was analyzed by x-ray diffraction on a four-circle diffractometer.[15] Cross-sectional and planar transmission electron microscopy (TEM) was used to examine the defect microstructure.

The temperature dependence of the resistivity $\rho(T)$ was measured by a conventional four-probe method on 100 μm wide microbridges which were patterned by standard photoresist lithography and chemical etching. The microbridges were aligned with the [100] and [010] directions of the $SrTiO_3(001)$ substrates. The two directions used in the resistivity measurement will be denoted by L and T, respectively, since they coincide with the directions longitudinal and transverse to straight step edges on the substrate and film surface. As will be shown in the following, these step edges are linked to the defect microstructure in the epitaxial films. Throughout this paper we will use zero resistivity $[\rho(T_c) \approx 0]$ to define the transition temperature T_c.

By means of the magneto-optical Faraday effect[16] (MOFE) the penetration of magnetic flux was visualized after cooling the film at zero-field from room temperature to liquid-He temperature and subsequently applying an external magnetic field (B_{ext}) perpendicular to the film plane. The samples were patterned by standard photoresist lithography and chemical etching into 2 mm $\times$ 2 mm squares with the edges aligned with the L and T directions. Because the HTSC's themselves exhibit only a weak Faraday effect, an iron-garnet film was placed directly on top of the sample as a field-sensing element. Thus, under crossed polarizers the flux carrying regions (Shubnikov states) appear bright, while the Meissner states are dark. In this way, we detect the local magnetic field with a lateral resolution of less than 10 μm.

III. STRUCTURAL PROPERTIES

A. Growth mode on vicinal surfaces

The heteroepitaxial growth of *c*-axis-oriented YBCO films on well-oriented $SrTiO_3(001)$ generally proceeds via formation of essentially three-dimensional islands on the pristine substrate surface for the Volmer-Weber growth or on a wetted substrate surface for coherent Stranski-Krastanov growth. The growth mode primarily depends on the lattice mismatch between $SrTiO_3$ and the HTSC material, the supersaturation (i.e., the excess of adsorbed particles on the substrate surface produced by the impinging flux), the surface and interface free energy as well as the surface diffusivity. Because surface steps and kinks are often higher binding energy locations (because of a higher coordination), they can act as preferred adsorption sites (at least for homoepitaxy). If the particles supplied by the impinging flux have sufficient mobility, they can diffuse to a step at a distance smaller than the diffusion length λ_s. Particles farther away from the surface step arrange themselves in epitaxial islands if the supersaturation on the terrace suffices to create nuclei with a critical radius.[17]

Surface steps and kinks are directly produced by vicinal off cut: a crystal surface misoriented slightly with respect to a low index direction displays terraces of low-index orientation and steps which accomodate the misorientation. As an example, Fig. 1(a) shows the UHV-annealed surface of 1.2° (off (001), toward [010]) miscut $SrTiO_3(001)$. Carefully annealed vicinal $SrTiO_3(001)$ surfaces are remarkable, since they exhibit step edges which are extremely straight and exclusively aligned along [100] and [010]. Furthermore, the terrace widths are almost constant, thus indicating repulsive step-step interactions. A cross section along the white line of Fig. 1(a) [see Fig. 1(b)] displays $\approx$18 nm wide (001) terraces separated by steps, mostly 0.39 nm high (corresponding to the $SrTiO_3$ unit cell height). Moreover, we observe some $\approx$37 nm wide terraces along with double unit-cell ($\approx$0.78 nm) high steps. This regular array of straight step edges running parallel to [100] dramatically affects the migration of deposited particles on the $SrTiO_3(001)$ surface. With a terrace width $\lambda < \lambda_s$, those particles form a smooth layer without reaching a supersaturation sufficient for nucleation of islands on the terraces and, thus, at the beginning a replica of the stepped substrate surface is generated; a process which we call self-organization. Consequently, the growth proceeds at the beginning similar to the typical step flow. The surface of a 120 nm thick YBCO film on 1.2° miscut $SrTiO_3(001)$ is shown in Fig. 1(c). It displays $\lambda^* = 100-130$ nm wide terraces generated by the self-organization of the YBCO. However, the film terraces are about six times larger than those of the clean substrate surface indicating a tendency to overgrow a fraction of the substrate steps. We shall return to this phenomenon in our subsequent discussion of the defect microstructure and morphology of YBCO films on $SrTiO_3(106)$.

Figure 1(c) shows a 45 nm $\times$ 75 nm large island on a 130 nm wide film terrace. The enlarged terrace width λ^* obviously led to the transition from step-flow growth to island formation. Even some growth islands consisting of stacks of terraces are detected in different surface regions of this YBCO film [see Fig. 1(d)]. The crossover terrace width λ^*

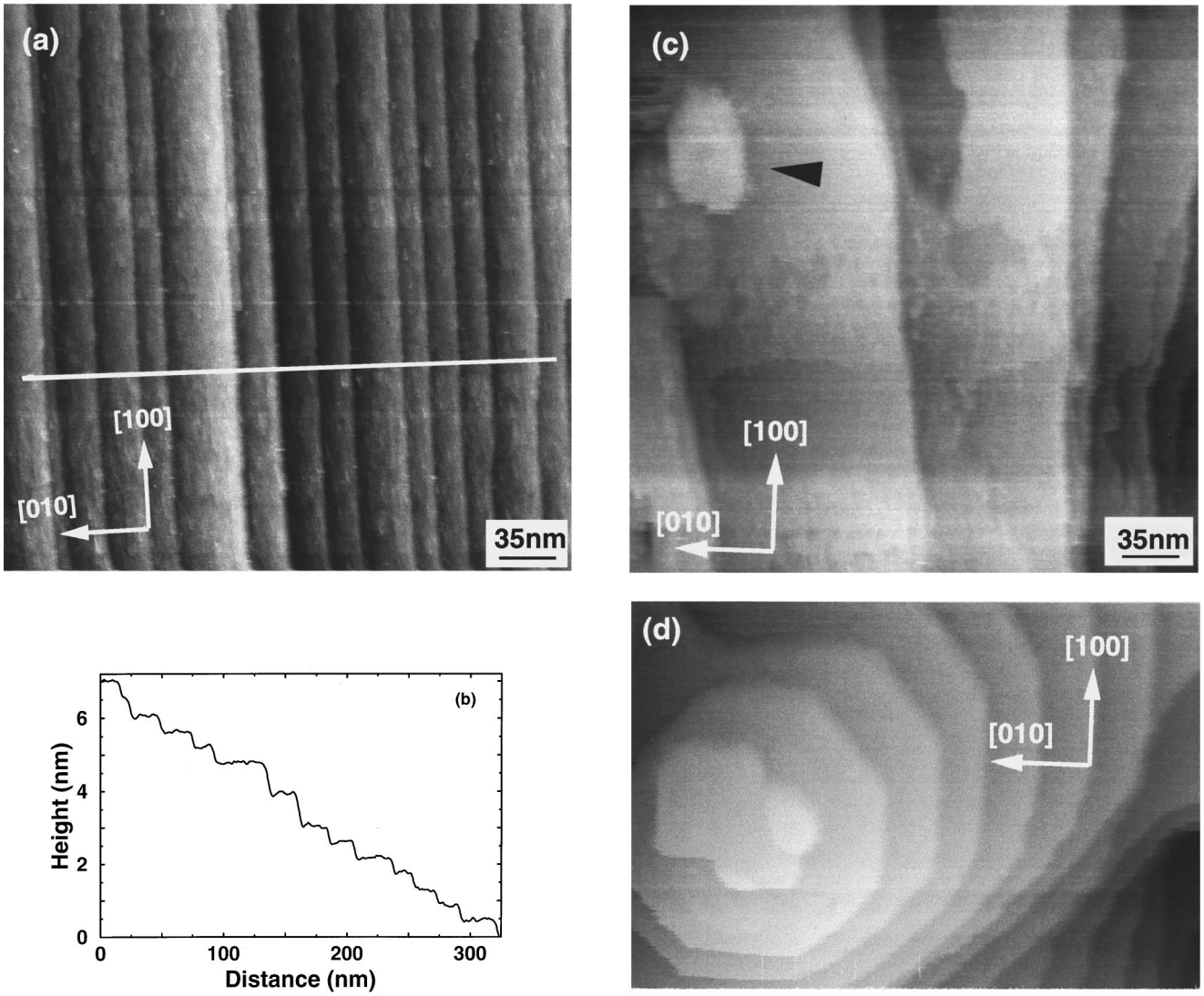

FIG. 1. (a) 350 nm × 350 nm UHV-STM image of vicinal $SrTiO_3$(001): The crystal was cut 1.2° off (001) toward [010]. (b) Cross section of the topography along the white line displayed in (a). (c) 350 nm × 350 nm UHV-STM image of a 120 nm thick YBCO film grown on the 1.2° miscut $SrTiO_3$(001) shown in (a). (d) Different surface region of the YBCO film displaying a concentric growth island.

must be close to the diffusion length λ_s for our chosen growth parameters, i.e., $\lambda_s \approx \lambda^* \approx 100$ nm.

Because kinks can act as the most favorable attachment sites for deposited particles (certainly for homoepitaxy), a substrate surface containing a large number of kinks leads to a dramatic change in the surface morphology of the adlayer. As an example, Fig. 2(a) shows the surface of 2.6° miscut $SrTiO_3$(001). The regular kink structure visible in this STM image appears when the miscut is toward [110]. A cross section along the white line in the STM image displays ≈35 nm wide (001) terraces separated by steps of different heights (1.17, 1.56, and 1.95 nm), all larger than the lattice constant of $SrTiO_3$ [see Fig. 2(b)]. The kinks appear to force step bunching. As can be seen from Fig. 2(c), this structure of the $SrTiO_3$ surface leads to a particular growth pattern of the YBCO film. The 60 nm thick layer exhibits elongated islands which terminate in ragged step edges. The shape of the islands is reminiscent of the kink structure of the clean substrate.

So far, we did not consider the influence of the mismatch between $SrTiO_3$ and the HTSC material on the growth mechanism. We are not dealing with homoepitaxy and YBCO building blocks which nucleate at steps must be strained to match $SrTiO_3$ in the (001) and (010) plane. UHV-STM studies[18] of YBCO nucleation on vicinal $SrTiO_3$(001) suggest that the nucleation mode depends on this strain and the chemical misfit. However, further investigations are needed to establish a conclusive picture of the nucleation process.

B. Tailored substrate surface

A crucial step to modify the transport properties and to enhance flux pinning in a controlled way is the structuring of the substrate surface. In the previous section, we have demonstrated a close relationship between the growth pattern of YBCO films and the substrate surface structure which strongly depends on the angle of misorientation θ, the miscut direction, as well as the temperature. Figure 3(a) shows the surface of 10° miscut $SrTiO_3$(001) after UHV annealing at 950°C. Because a sufficient mobility (diffusivity) of surface atoms is needed for structural changes to occur, we expect

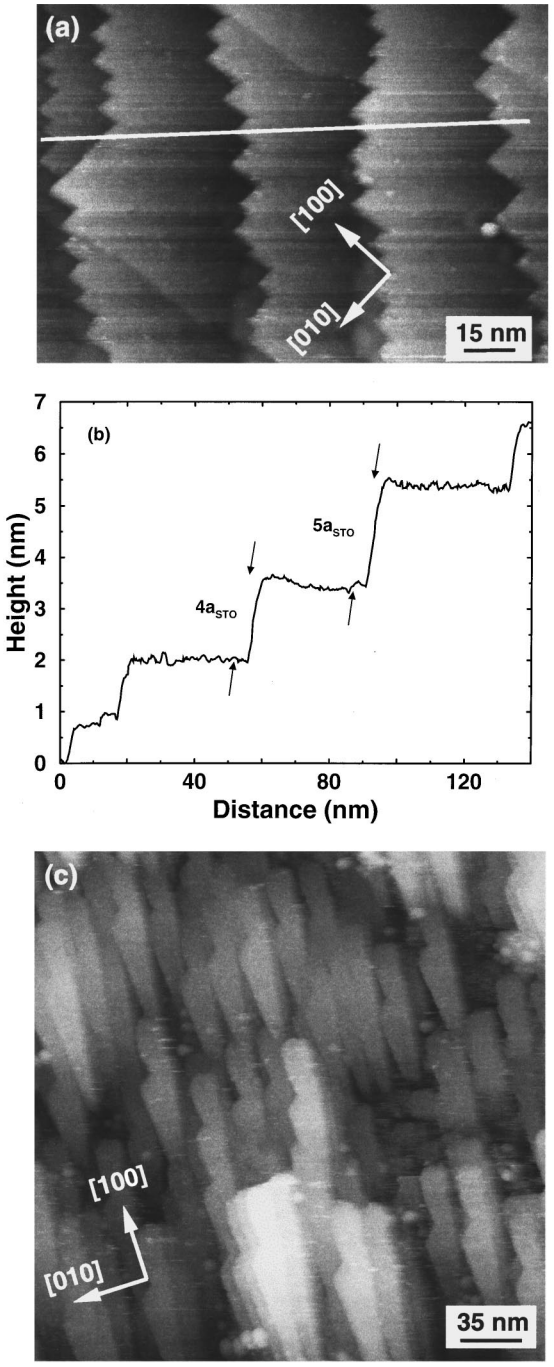

FIG. 2. (a) 150 nm × 100 nm UHV-STM image of vicinal $SrTiO_3(001)$: The crystal was cut 3° off (001) toward [110]. (b) Cross section of the topography along the white line displayed in (a). (c) 350 nm × 350 nm UHV-STM image of a 60 nm thick YBCO film grown on the 3° miscut $SrTiO_3(001)$ shown in (a).

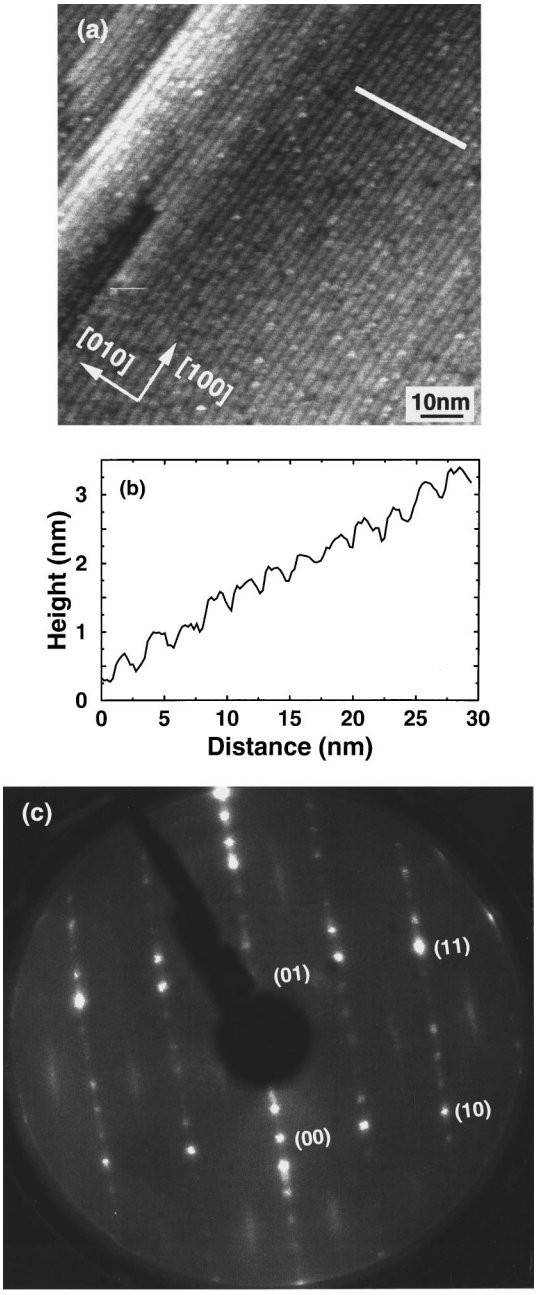

FIG. 3. (a) 100 nm × 100 nm STM image of $SrTiO_3(106)$ after UHV annealing (see text). (b) Cross section of the topography along the white line displayed in (a). (c) Corresponding LEED pattern (electron energy = 42 eV).

that the surface structure will be freezing in at some temperature while cooling the sample from 950 °C to room temperature. Therefore, the UHV-STM image acquired at room temperature reflects a surface structure at some higher freezing-in temperature. As can be seen from the cross section of the topography in Fig. 3(b), the periodic row-like structure visible in Fig. 3(a) consists of 2.3 nm wide $SrTiO_3(001)$ terraces separated by straight steps in the [010] direction, mostly 0.39 nm high. This finding implies that the regular nanoscale terraces are comprised of six $SrTiO_3$ unit cells, i.e., under our preparation conditions a stable $SrTiO_3(106)$ surface is generated which appears to exhibit $6 \times a_{SrTiO_3}$ wide (001) terraces separated by unit-cell high steps. The LEED pattern shown in Fig. 3(c) is characteristic of a single domain (2×6) reconstruction, but displays a characteristic modulation of the spot intensities. The diffraction pattern of a periodic array of terraces is determined by the atomic reconstruction on the terrace and periodic arrangement of the steps. Because the periodicity of the nanoscale step structure equals the lattice constant of $SrTiO_3$ multiplied by six, we suggest that the observed LEED pattern results from a convolution of the scattering amplitude due to the periodic array of steps and a (2×2) reconstruction in the

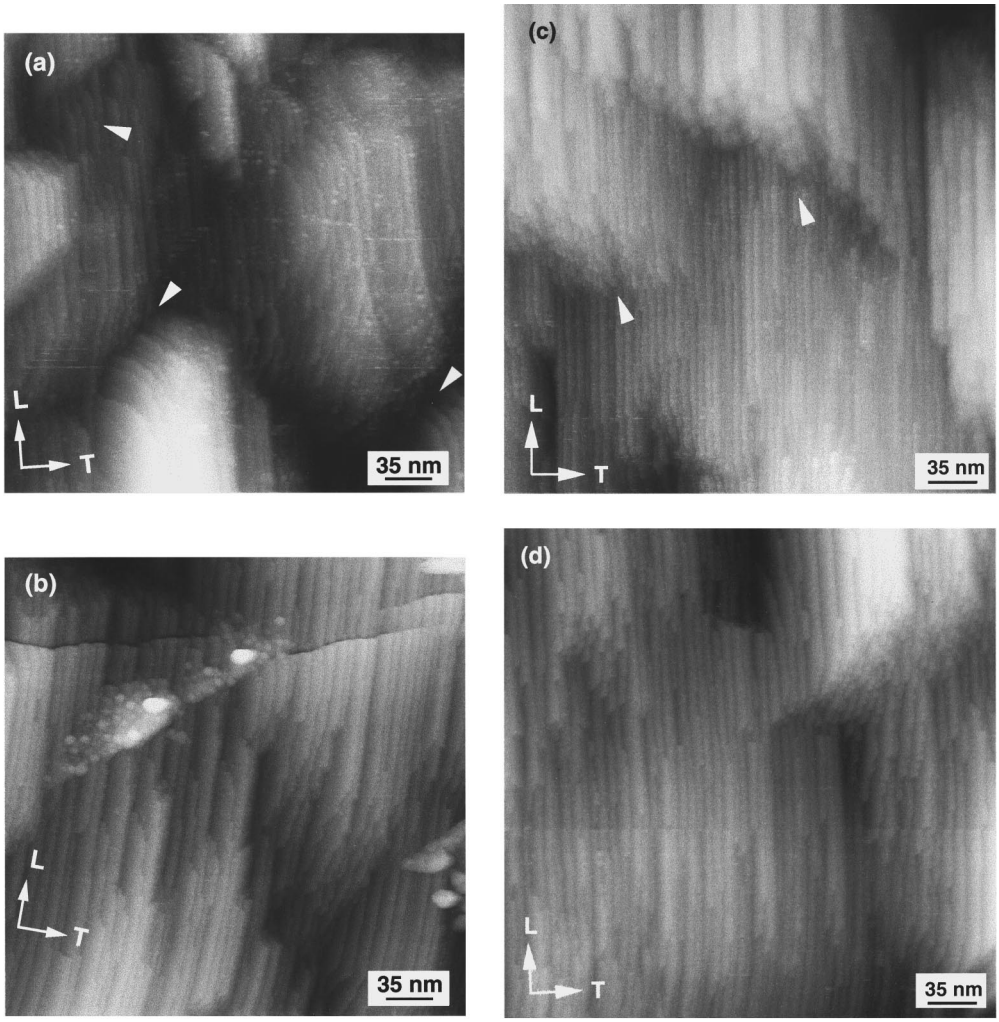

FIG. 4. 350 nm × 350 nm STM images of (a) 24 nm, (b) 60 nm, (c) 120 nm, and (d) 240 nm thick YBCO films grown on UHV-annealed $SrTiO_3$(106). Arrowheads indicate (a) local disruptions of the terrace structure and (c) ragged step edges referred to in the text. The two directions used in transport measurements are denoted by T and L. (e) Cross section of the topography of the 24 nm thick film along the white line shown in (a).

[100] direction on the terrace [along the step edges, see Fig. 3(c)]. Reconstructions with a twofold periodicity are actually frequently observed[19,20] on $SrTiO_3$(001).

As demonstrated in the previous section, the uniformly spaced steps and the straight step edges of the vicinal surface are expected to promote self-organization of the adlayer in a particular efficient way. Because the 0.39 nm high $SrTiO_3$ steps are only a fraction of the YBCO unit cell along its c axis ($c \approx 1.2$ nm), dislocations are presumably formed at the step edges. Therefore, we have generated a substrate surface ideally suited to introduce an array of determined density of defects into epitaxial YBCO films in a controlled way.

C. Growth morphology on $SrTiO_3$(106)

The STM images of YBCO-covered $SrTiO_3$(106), shown in Fig. 4, reveal the evolution of the layer morphology with increasing film thickness t. The growth pattern differs distinctly from the morphology of YBCO films on well-oriented $SrTiO_3$(001) which displays square islands or spiral growth features, depending on the substrate preparation and growth conditions. In Fig. 4(a), we find nanoscale terraces reminescent of those of the clean substrate surface. They are separated by straight steps along [100] (i.e., they are aligned with the steps on the clean $SrTiO_3$ surface). In the following, the directions which are longitudinal and transverse to these step edges will be called L and T, respectively. With $t = 24$ nm, the terraces are frequently interrupted in the L direction [i.e., the film thickness is not homogeneous in this direction and the film exhibits islandlike features; see Fig. 4(a)]. Furthermore, the terrace lengths are fairly periodic along the T direction. As can be seen from Figs. 4(b)–4(d), the YBCO nanoscale terraces become continuous in the L direction as growth proceeds. Moreover, the width distribution of the terraces becomes more regular, almost periodic (for a detailed discussion of this issue, we refer to a previous publication[21]). However, even with $t > 60$ nm, we observe some nanoscale terraces of finite length in the L direction which terminate in ragged steps with their edges aligned along the T direction [see Fig. 4(c)].

We suggest different sources of the local discontinuity of the terrace structure. Although not directly imaged by STM, a small number[22] of Y_2O_3 precepitates has been found by cross-sectional TEM. The growth front might be pinned by

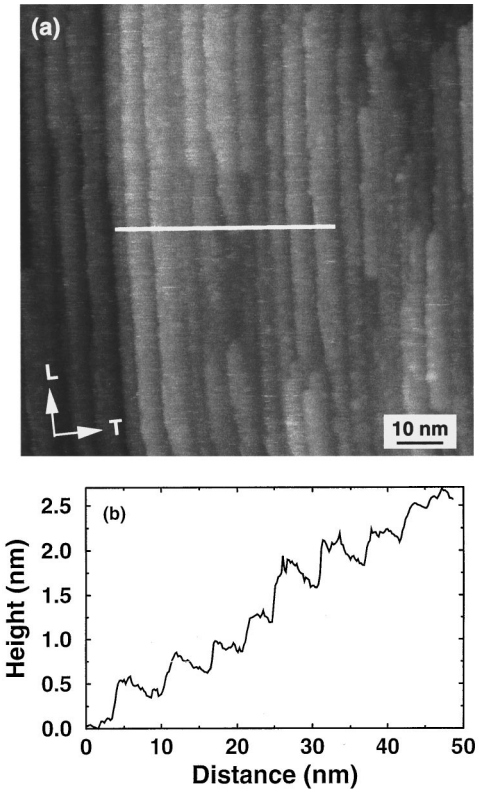

FIG. 5. (a) 100 nm × 100 nm STM image of a 240 nm thick YBCO film grown on UHV-annealed $SrTiO_3$(106). (b) Cross section of the topography along the white line displayed in (a).

this off-stoichiometric material. Furthermore, the discontinuity of the YBCO terraces might be related to strain fields in the vicinity of growth-related defects. We have shown in the previous section that kinks on the substrate surface lead to the formation of elongated cigarlike islands terminating in ragged step edges. Thus, also the existence of kinks resulting from a small additional miscut in the L direction can be responsible for the observed local discontinuity of the terraces.

The STM image of Fig. 5(a), shows on a smaller scale an almost periodic array of YBCO terraces on the surface of the 240 nm film. This periodic morphology originates from self-organization of YBCO enabled by the particular growth kinetics on the terraced $SrTiO_3$ surface.[21] The profile of the topopraphy in Fig. 5(b) shows straight step edges spaced 4–7 nm apart and growth steps of different heights, all less than $c_{YBCO} \approx 1.2$ nm [see also Fig. 6(a)]. These findings imply that antiphase boundaries (APB's) with a planar structure are formed upon coalescence of domains nucleating on adjacent terraces which are shifted vertically by 0.39 nm [see schematic illustration in Fig. 6(b)]. Because ≈0.6 and ≈0.8 nm high growth steps are observed, we also expect some stacking faults (SF's) along the c axis. The fact that the regular film terraces are 2–3 times wider than those of the clean substrate suggests a partial overgrowth of $SrTiO_3$ steps. This observation is consistent with the existence of a variable stacking mode on the $SrTiO_3$ surface recently proposed by Zegenhagen *et al.*[23] (see following section).

D. Epitaxy and defect microstructure

The growth pattern of YBCO films on $SrTiO_3$(106) implies a characteristic defect structure. Figure 7(a) shows a

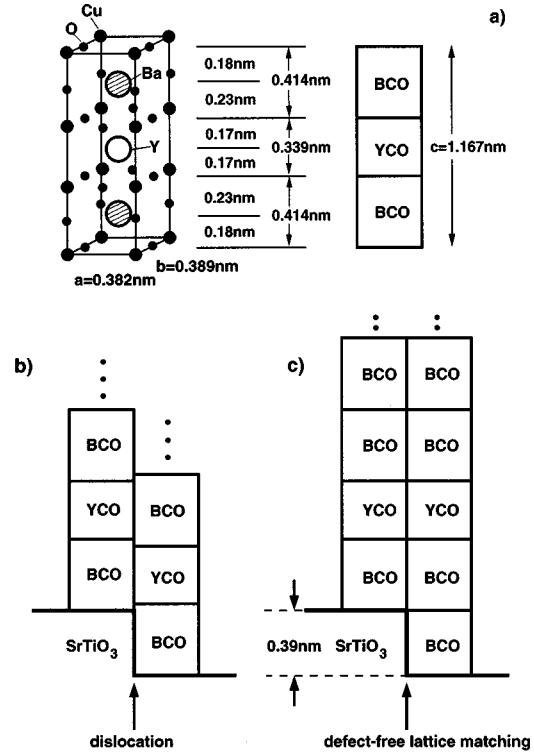

FIG. 6. (a) Unit cell of $YBa_2Cu_3O_{7-\delta}$ and its schematic representation as three perovskitelike blocks. (b) Illustration of the formation of an antiphase boundary at a substrate step: domains nucleating on adjacent terraces are shifted vertically by a fraction of the unit cell. (c) A change of the stacking sequence on adjacent terraces allows a smooth and defect-free overgrowth of a substrate step.

TEM image (cross section along the T direction) of a YBCO film on $SrTiO_3$(106). The periodicity of the YBCO lattice is strongly disturbed. CuO planes visible as bright lines are frequently interrupted, shifted vertically, or even slightly bent. Continuous, undisturbed planes exist only up to a length (in the T direction) of about 6–8 nm. The extent of this disorder renders the identification of individual defects more difficult. In particular, the substrate/film interface appears to be slightly out of focus, but we can still identify the descending sequence of $SrTiO_3$ steps along [010] (T). The c axis of the material is oriented perpendicular to the $SrTiO_3$(001) terraces, as corroborated by x-ray diffraction.

The large scale micrograph, Fig. 7(a), contains numerous APB's, directly arising from mostly 0.39 nm (and some 0.78 nm) high substrate steps which are shorter than the YBCO unit cell along its c axis ($c \approx 1.2$ nm). However, the APB's are healed after a few unit cells from the substrate surface by inclusion of SF's lying in the (001) plane [see also Fig. 7(b)]. Moreover, the number of APB's is smaller than that of the $SrTiO_3$ steps, indicating the tendency to overgrow a fraction of substrate steps. This scenario might be made possible by a variable stacking mode at the interface. Our recent results from x-ray standing wave measurements[23] suggested the existence of this mechanism: on a TiO_2 terminated $SrTiO_3$ surface, the stacking sequence starts with TiO_2-BaO-CuO_2-Y-CuO_2-BaO-CuO-· · · or TiO_2-BaO-CuO-BaO-CuO_2-Y-CuO_2-· · ·. The variable stacking mode reduces the number of APB's initiated from the substrate steps, as schematically illustrated in Fig. 6(c), and permits a defect-free

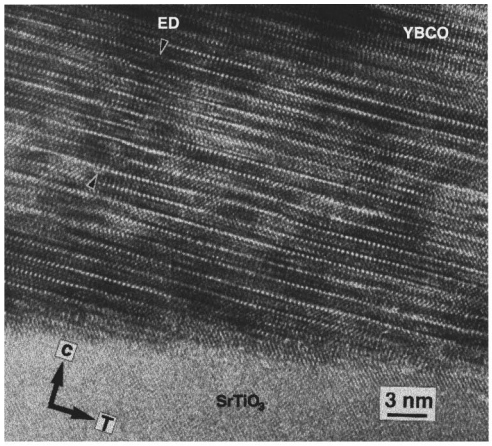

(a)

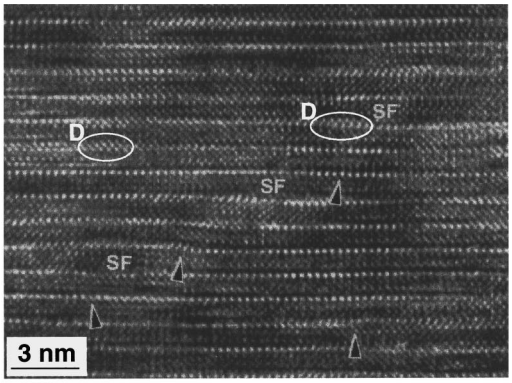

(b)

FIG. 7. (a) High-resolution cross-section TEM image along the *T* direction showing numerous antiphase boundaries (APB). An extended defect (ED) referred to in the text is marked by arrowheads. (b) Section of the TEM image showing the formation of APB's (some of them are marked by arrows) away from the substrate/film interface; some regions in which the CuO_2 planes appear to overlap are marked by *D*.

matching of the following upper layers, thereby reducing the free energy of the heteroepitaxial system.

Additionally, we observe APB's several nanometers away from the substrate/film interface [see Fig. 7(b)]. They are generated during coalescence of growth fronts, which nucleate on adjacent YBCO terraces out of registry with one another. After a few unit cells, the mostly curved APB's are terminated by a SF. Figure 7(a) also shows an APB with a vertical shift of $c/3$ in conjunction with a ≈ 2 nm wide distorted region. This extended defect (marked by arrows in the TEM micrograph), which presumably leads to a local depression of the superconducting order parameter, persists over several unit cells along [001]. However, most APB's exhibit a structural width of less than 1 nm. The atomic planes across the boundary can be slightly tilted, a fact which indicates strain associated with the large density of defects. We also observe some regions in which CuO planes appear to overlap [see Fig. 7(b)].

Because the APB's originate from self-organization of YBCO on the terraced $SrTiO_3$ and YBCO surface, respectively, we expect planar defects, aligned with the direction of the straight step edges (L). Planar-view TEM confirms the

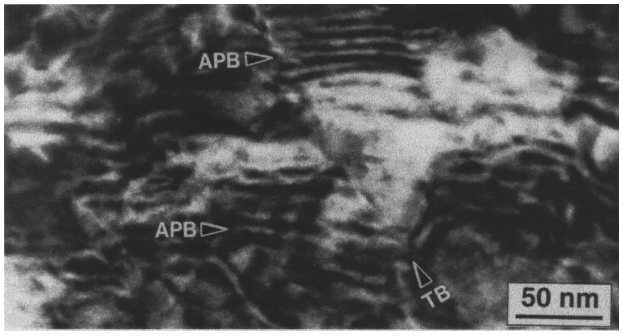

FIG. 8. Low-magnification planar-view TEM image showing a strong diffraction contrast due to antiphase boundaries (APB) and twin boundaries (TB).

anisotropic nature of the defect microstructure. As a consequence of the large density of defects, the low-magnification [001] planar-view TEM image in Fig. 8 shows a strong diffraction contrast. Since APB's are mostly curved and formed incoherently within the layering sequence [see Fig. 7(c)], the image contrast reflects a projection of various defects, rather than features from an individual boundary. However, in some regions we can clearly resolve a regular intensity pattern with bright lines almost parallel to [100]. Since the period of these lines is comparable to the width of the YBCO terraces shown in Fig. 5, we attribute this pattern to growth-related APB's, which are aligned with straight step edges of the substrate and film surface, respectively. Moreover, the planar-view TEM image contains some twin boundaries (TB) along [110] and $[\bar{1}10]$, traversing the planar APB's.

Figure 9 shows a TEM image (cross section along the *T* direction) of a YBCO film on 1.2° miscut $SrTiO_3$. The density of defects is significantly reduced compared to YBCO films on $SrTiO_3$(106). Furthermore, the APB's at the substrate/film interface persist over a large fraction of the film thickness without being healed by inclusion of SF's. It is worth mentioning, that CuO chains and CuO_2 planes are partially broken across an APB in the *T* direction, but mostly continuous in the *L* direction. We therefore expect different transport properties along the *L* and *T* directions. Moreover, the observed defects with a different shape and structural width in YBCO films on $SrTiO_3$ substrates with different vicinal angle should act as pinning centers with varying efficiency.

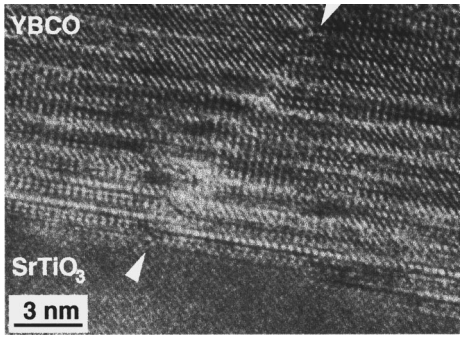

FIG. 9. High-resolution cross-section TEM image along the *T* direction showing an extended antiphase boundary (APB) marked by arrowheads.

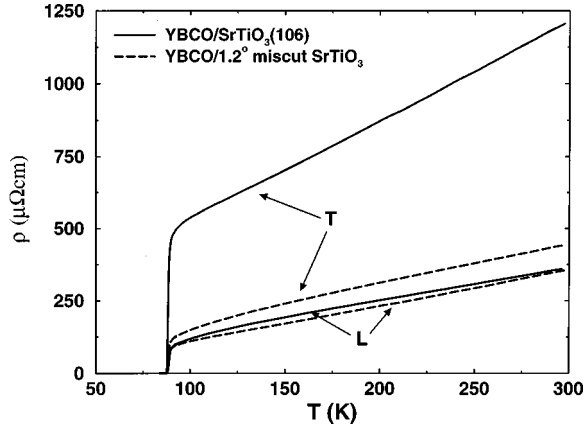

FIG. 10. Resistivity $\rho_{T,L}$ in the T and L directions (see text) versus temperature for 120 nm thick YBCO films on $SrTiO_3(106)$ (solid line) and 1.2° (toward [010]) miscut $SrTiO_3(001)$ (dashed line).

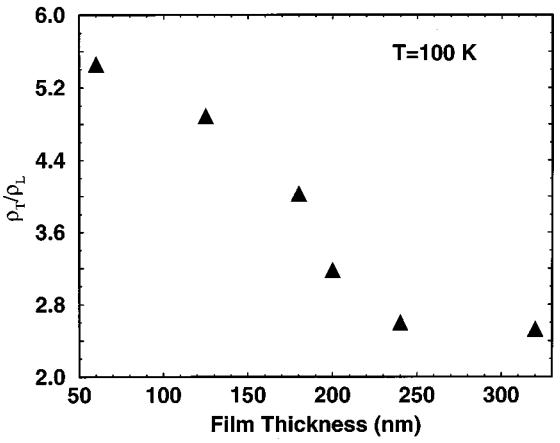

FIG. 11. Resistivity anisotropy $A_\rho(10°,100\ \mathrm{K})=\rho_T/\rho_L$ at 100 K versus film thickness for YBCO films on $SrTiO_3(106)$.

IV. TRANSPORT IN THE NORMAL AND SUPERCONDUCTING STATE

A. Defect-related shift of the transition temperature

Figure 10 shows the resistivity of 120 nm thick YBCO films on $SrTiO_3(106)$ and 1.2° miscut $SrTiO_3(001)$ in the L and T directions. The resistive transition temperature T_c of various 120 nm thick films on $SrTiO_3(106)$ ranges between 87 and 88 K. It is slightly reduced compared to YBCO films grown on almost atomically flat $SrTiO_3(001)$ substrates under identical conditions ($T_c \approx 90$–91 K). The T_c of YBCO is known to depend on the oxygen stoichiometry and specific ordering of oxygen atoms in the basal CuO planes.[24] The position of the A_{1g} mode in the Raman spectrum of YBCO films on $SrTiO_3(106)$ suggests fully oxygenated material.[25] Therefore, the reduction of T_c must be related to the growth-related defects.

Modeling the influence of defects on T_c quantitatively using Abrikosov-Gor'kov pair-breaking theory[26] would require assumptions about the pairing symmetry (d or s wave) of HTSC's and the magnetic moments of the defects. Since these issues are still controversial, we provide a rough estimate of the number of defects necessary to cause the observed shift δT_c of the transition temperature. Considering only defects at which the order parameter is reduced, we can model the interface between a defect and the superconducting matrix as a normal-superconducting interface.[27] With this approximation the relative T_c suppression is given by

$$\delta T_c / T_{c0} = \left(\frac{\pi \xi_{ab}(0)}{2s} \right)^2, \tag{1}$$

where $T_{c0} \approx 93$ K is the transition temperature of the defect-free material, $\xi_{ab}(0) \approx 1.5$ nm is the Ginzburg-Landau coherence length, and s is the average distance between defects. With $\delta T_c \approx 5$ K in YBCO on $SrTiO_3(106)$ we find $s \approx 10$ nm, a value a little larger than the spacing of ≈ 6 nm between defects as revealed by combined STM and TEM data. Within the frame of the chosen model, this finding suggests that the order parameter is not necessarily depressed at each of the observed APB's.

For comparison, the transition temperature of various 120 nm thick YBCO films on 1.2° miscut $SrTiO_3(001)$ does not differ from the value observed in YBCO films grown on almost atomically flat $SrTiO_3(001)$ substrates under identical conditions.

B. Resistivity anisotropy

As can be seen from Fig. 11, the YBCO films on $SrTiO_3(106)$ exhibit a resistivity anisotropy between the L and T direction which strongly depends on the film thickness. The resistivity $\rho_{L,T}$ at 100 K, as well as the corresponding anisotropy ratio $A_\rho(100\ \mathrm{K}) = \rho_T(100\ \mathrm{K})/\rho_L(100\ \mathrm{K})$ for each sample are also listed in Table I. With decreasing film thickness t, $A_\rho(100\ \mathrm{K})$ increases from ≈ 2.5 at $t = 320$ nm to ≈ 5.5 at $t = 60$ nm (see Fig. 11).

The orthorhombicity of YBCO, i.e., the existence of conducting CuO chains between the pairs of CuO_2 planes (along a direction denoted as b), leads to an *intrinsic* anisotropy of charge transport in the *ab* plane which has been found to vary nearly linearly with temperature ($\rho_a/\rho_b \approx 2.2$ between 150 and 275 K).[28] Therefore, $A_\rho(T)$ cannot be attributed to the intrinsic anisotropy of the in-plane resistivity which is also not present in twinned samples. The YBCO films grown on the perodically stepped $SrTiO_3(106)$ surface are twinned.[15]

In order to understand the measured anisotropy A_ρ, we first examine the transport properties of a fictitious defect-free film, in which the YBCO unit cells are tilted with respect to the macroscopic film and substrate surface [i.e., the (106) plane]. We shall add the contributions of defect scattering in the subsequent discussion. In the T direction, we expect a complicated zig-zag current path along and perpendicular to the CuO_2 planes and the CuO chains. We model the macroscopic current as flowing through a network of resistors linked in series representing the in- and out-of-plane contributions to the current path, which are determined by the tilt angle θ. In this simple model the effective resistivity of the fictitious film in the T direction can be deduced according to the expression

$$\rho_T(\theta, T) = \rho_c(T) \sin^2\theta + \rho_{ab}(T) \cos^2\theta, \tag{2}$$

TABLE I. Summary of linear fit parameters, $\rho(T)=\rho_0+\alpha T$ for 100 K $<T>$ 290 K, resistivities at 100 K and resistivity anisotropies $A_\rho=\rho_T/\rho_L$ for YBCO films on $SrTiO_3(106)$ with different thicknesses t. The subscripts T and L indicate the $[60\bar{1}]$ and [100] crystallographic directions as defined in the text.

Sample	t (nm)	$\rho_{0,L}$ ($\mu\Omega$ cm)	α_L	ρ_L(100 K) ($\mu\Omega$ cm)	$\rho_{0,T}$ ($\mu\Omega$ cm)	α_T	ρ_T(100 K) ($\mu\Omega$cm)	A_ρ
A	60	11.2	1.39	145	455	3.32	793	5.5
B	125	−12.3	1.23	110	199	3.30	538	4.9
C	180	−14.6	1.08	99	137	2.59	398	4.0
D	200	−6.6	0.95	86	105	1.60	266	3.1
E	240	−22.5	0.91	71	28.7	1.58	188	2.6
F	320	−25.3	0.85	57	9.5	1.17	144	2.5

where ρ_{ab} and ρ_c are the *intrinsic* in- and out-of-plane resistivities of YBCO. Further, if we assume that the current in the L direction essentially flows along the CuO_2 planes and the CuO chains, ρ_L is given by

$$\rho_L(T)=\rho_{ab}(T). \tag{3}$$

Using Eqs. (2) and (3), we obtain the resistivity anisotropy of the fictitious film:

$$\tilde{A}_\rho(\theta,T)=\cos^2\theta+[\rho_c(T)/\rho_{ab}(T)]\sin^2\theta. \tag{4}$$

To calculate $\tilde{A}_\rho(10°, 100\ \mathrm{K})$, we use the intrinsic anisotropy ratios $\rho_c/\rho_a(100\ \mathrm{K})\approx 63$ and $\rho_c/\rho_b(100\ \mathrm{K})\approx 120$ measured by Friedmann *et al.*[28] in a twin-free crystal of YBCO. Our model neglects contributions from twin boundaries and other defects. However, in order to account for twinning of our films, we assume that ρ_{ab} contains isotropic contributions from both, the CuO_2 planes and the CuO chains. We can calculate ρ_{ab} by taking the geometric mean of ρ_a and ρ_b. In this model of transport in a fictitious defect-free YBCO film with CuO_2 planes tilted 10° with respect to the surface, the anisotropy ratio is $\tilde{A}_\rho(10°, 100\ \mathrm{K}) = 3.6$.

As can be seen in Fig. 11, the resistivity anisotropy $A_\rho(100\ \mathrm{K})$ of the YBCO films on $SrTiO_3(106)$ is reduced with increasing film thickness and appears to be constant for film thicknesses larger than 200 nm. In contrast, Eq. (4), which only accounts for a combination of in- and out-of-plane transport, yields a thickness-independent anisotropy $\tilde{A}_\rho$. Therefore, the measured resistivity anisotropy A_ρ cannot be entirely attributed to some additional c-axis resistivity for transport in the T direction. Because (i) $\rho_{ab}(100\ \mathrm{K})=(\rho_a\rho_b)^{1/2}=30\ \mu\Omega\mathrm{cm}$, incorporated in Eq. (4) falls below typical values of the best twinned crystals and (ii) the c-axis conductivity may be enhanced by interplanar disorder,[29] Eq. (4) overestimates the anisotropy resulting from c-axis transport in the T direction. However, there is no doubt that in the thin films on $SrTiO_3(106)$ the dominant contribution to the resistivity anisotropy originates from the defect miscrostructure.

Figure 12 displays the resistivity anisotropy $A_\rho(\theta,100\ \mathrm{K})$ of 120 nm thick YBCO films grown on vicinal $SrTiO_3(001)$ substrates with different tilt angle θ. $A_\rho(\theta,100\ \mathrm{K})$ increases from ≈ 1 at $\theta\approx 0°$ to ≈ 4.9 at $\theta\approx 10°$. To compare the measured $A_\rho(\theta,100\ \mathrm{K})$ data with the model of transport in a fictitious film described above, we use $\rho_c/\rho_{ab}(100\ \mathrm{K})=53.4$ as derived from the anisotropy ratio $A_\rho(100\ \mathrm{K})\approx 2.5$ for the 320 nm thick YBCO film on $SrTiO_3(106)$ as a representative value of the effective intrinsic anisotropy ratio $\rho_c/\rho_{ab}(100\ \mathrm{K})$ in our films. However, even $A_\rho(100\ \mathrm{K})\approx 2.5$ is likely to be influenced by twin boundaries, translational boundaries and stacking faults revealed by TEM. As can be seen from Fig. 12, the $\tilde{A}_\rho(\theta,100\ \mathrm{K})$ data calculated from Eq. (4), differ significantly from the experimental data. This finding confirms the dominant contribution of the defect microstructure to the resistivity anisotropy. It is reasonable to relate the dependence of the anisotropy ratio on θ to an increasing density of defects with decreasing substrate terrace width and correspondingly increasing tilt angle θ.

C. Systematics of $\rho(T)$

The resistivity anisotropy between the L and T directions, described in the previous section is correlated with the anisotropic nature of the defect microstructure revealed by combining the STM and TEM data. By investigating the systematics of $\rho_L(T)$ and $\rho_T(T)$ as a function of film thickness we gain insight into the interplay between growth-related defects and charge transport in epitaxial films. In the following, we focus on YBCO films on $SrTiO_3(106)$.

The measured $\rho_L(T)$ data can all be accurately fitted by

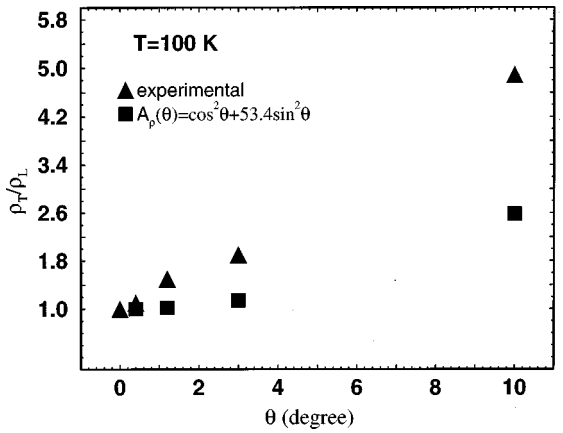

FIG. 12. Resistivity anisotropy $A_\rho(\theta,100\ \mathrm{K})=\rho_T/\rho_L$ at 100 K versus tilt angle θ for 120 nm thick YBCO films on vicinal $SrTiO_3(001)$ substrates. Triangles represent experimental data, squares calculated data based on a model of combined in- and out-of-plane transport (see text).

$$\rho(T)=\rho_0+\alpha T, \tag{5}$$

where ρ_0 is the residual resistivity which is generally ascribed to static disorder (defects) and α represents the slope $d\rho/dT$, where $\rho(T)$ is a linear function of temperature. Evidence for a deviation from the T-linear behavior is noted in the transverse direction, if t falls below 60 nm: $\rho_T(T)$ is linear for 150 K $< T >$ 200 K, but shows a superlinear upturn for $T\rightarrow 300$ K and $T\rightarrow 100$ K. Table I summarizes the fits to the resistivity data for each sample. With decreasing film thickness t, we find a systematic increase of ρ_0, $\rho(100$ K) and α in both directions.

At 100 K, the resistivity ρ_L of the 320 nm thick YBCO film on $SrTiO_3(106)$ is exceptionally small: $\rho_L(100\ \mathrm{K}) \approx 57\ \mu\Omega\,\mathrm{cm}$ falls below the value of $\approx 90-200\ \mu\Omega\,\mathrm{cm}$ typically observed in twinned single crystals of YBCO and epitaxial films grown on well-oriented $SrTiO_3(001)$.[31] Furthermore, the linear fit to the normal-state resisitivity of this film yields a negative zero-temperature intercept ρ_0 as well as a remarkably small slope $\alpha \approx 0.85\ \mu\Omega\,\mathrm{cm/K}$. It is instructive to compare the thin-film data with the magnitude and T dependence of ρ_a and ρ_b in untwinned single crystals of YBCO.[28] While ρ_a(T) extrapolates to negative values for $T\rightarrow 0$ ($\rho_{0,a}\approx -14\ \mu\Omega$ cm), ρ_b(T) shows a vanishingly small residual resistivity. The slope $\alpha_L \approx 0.85\ \mu\Omega\,\mathrm{cm/K}$ of the film resisitvity is only 1.5 times (3.4 times) larger than that of $\rho_a(T)$ $[\rho_b(T)]$. Note that $\alpha \approx 2-3\ \mu\Omega\,\mathrm{cm/K}$ is typically observed in thin films of YBCO on $SrTiO_3$. It is evident that $\rho_L(T)$ approaches the behavior for single-crystal specimens. Our findings suggest that only some twin boundaries contribute to the resistivity along the current path in the L direction. However, with decreasing film thickness t, ρ_L is enhanced and the zero-temperature intercept turns from negative to positive values.

The $\rho_T(T)$ data from the 60 nm thick film on $SrTiO_3(106)$ reflect transport properties markedly different from those of single-crystalline bulk material. The magnitude of $\rho_T(100\ \mathrm{K})$ exceeds the values generally observed in YBCO thin films. In particular, the residual resistivity $\rho_{0,T}=455\ \mu\Omega\,\mathrm{cm}$ clearly indicates a strong contribution of static disorder to the scattering of charge carriers. With $\alpha=3.3\ \mu\Omega\,\mathrm{cm/K}$, as derived from the $\rho_T(T)$ data, this sample exhibits a slope characteristic of epitaxial YBCO films, but significantly smaller than that of a single crystal along the c axis ($\alpha=12.5\ \mu\Omega\,\mathrm{cm/K}$).[28] However, the exceptionally large resisitivity in the T direction is reduced with increasing film thickness.

From the evolution of the growth morphology described in the previous section, it is reasonable to relate the systematic changes in $\rho_{L,T}(T)$ with t to a thickness-dependent defect microstructure. We expect the nonvanishing residual resistivity to originate from different types of defects. We assume that twin boundaries along [110] and $[\bar{1}10]$, as well as possibly randomly distributed point defects contribute to the resistivity in both directions. A different situation occurs if point defects accumulate at APB's. We attribute the large resistivity in the transverse direction to APB's generated during coalescence of growth fronts at different stages of growth. Since we observe a defect-free overgrowth of steps and a healing of APB's via SF's, the number of defects and consequently their influence on charge transport is reduced with increasing film thickness. The observed SF's presumably affect the out-of-plane resistivity. Several models of c-axis conductivity are based on the existence of disorder which, e.g., enables tunneling through localized states.[29] However, our experiments do not permit us to elucidate the mechanism of c-axis transport.

A striking feature of the normal-state resistivity is the marked difference in the slope of the two $\rho(T)$ branches corresponding to the L and T directions, respectively. It is generally believed that static disorder affects the residual resistivity ρ_0, but not the slope α of $\rho(T)$ (at least for metals). Thus, the fact that ρ_0 and α simultaneously change with varying film thickness suggests that the observed defect microstructure affects the T-dependent carrier-boson scattering. However, the systematics of $\rho(T)$ can be modeled as resulting from charge transport in an effective medium: The resistivity in the T direction can be fitted reasonably well by the resistivity in the L direction according to the relation[30]

$$\rho_T(T)=C_1\rho_{\mathrm{APB}}+C_2[\rho_{0,L}+\alpha_L T], \tag{6}$$

where $C_1<1$ and $C_2>1$ are dimensionless geometric factors which depend on the volume fraction as well as the spacing of the APB's. The first term results from a fraction of the transport current which directly crosses the APB's, assuming that they contribute a finite resistivity ρ_{APB}. The second term is obtained if we model the transport current in the T direction as additionally flowing parallel through an APB and APB-free material. In particular, $[\rho_{0,L}+\alpha_L T]$ is the resistivity on the terrace which has been chosen to be the same in the L and T directions. In the limiting case where some of the observed defects exhibit an infinite resistivity the second term also accounts for the effect of locally varying cross sections and a lengthening of the current path, since the transport current will flow around such extended defects. Therefore, the difference in the slope of the two $\rho(T)$ branches may originate from percolation.

V. FLUX PINNING

A. Experimental results

1. Flux penetration into samples of square shape

After zero-field cooling a type-II superconductor and a successive application of external magnetic fields B_{ext} perpendicular to the sample surface, quantized flux enters the superconductor in the partly penetrated Shubnikov phase. Because pinning forces act on the individual vortices, the magnetic flux cannot fill up the sample homogeneously. Consequently, flux fronts are formed. The gradient and curvature of the magnetic flux in the sample generate a current density $\mathbf{j}(\mathbf{r})$ that takes the maximum possible value $|\mathbf{j}(\mathbf{r})|=j_c$. For the partly penetrated state, an additional screening current $|\mathbf{j}_s|<j_c$ in the flux-free zone compensates the self-field generated by the macroscopic current $\mathbf{j}(\mathbf{r})$ in the flux-carrying region. $\mathbf{j}(\mathbf{r})$ has to satisfy the continuity equation $\nabla\cdot\mathbf{j}(\mathbf{r})=0$ (no drains and sources) and has to flow parallel to the sample edges. As a consequence of these constraints, the current lines exhibit sharp bends forming discontinuity lines along the diagonals of the square. At these lines the orientation of the current changes discontinously,

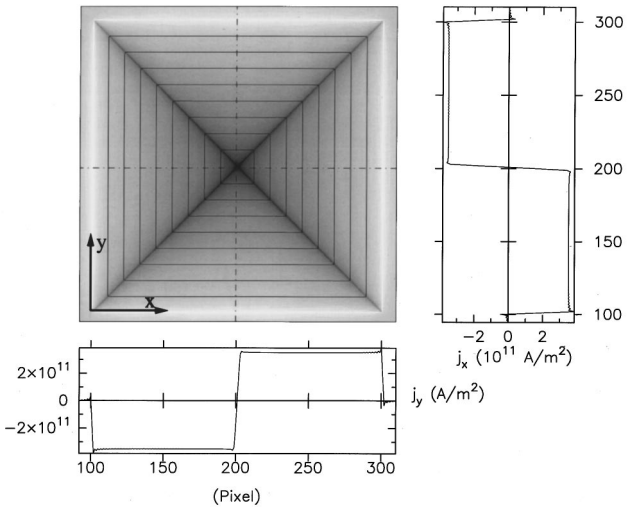

FIG. 13. Calculated flux density distribution in a homogeneous, c-axis-oriented YBCO film of square shape. Lines indicating the current path are superimposed on the grayscale image (more black corresponds to lower flux). Current profiles display the critical current densities j_x and j_y along the dashed lines in the x and y directions. The modified Bean model results in a constant critical current density for the fully penetrated state under consideration.

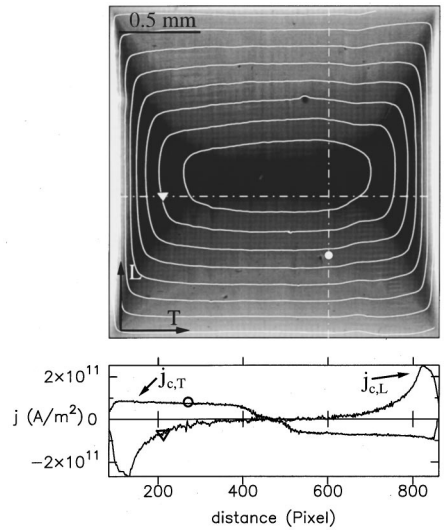

FIG. 14. Magneto-optically observed flux density distribution in a square-shaped, 360 nm thick YBCO film on $SrTiO_3$(106) at 32 mT and 4.2 K. Lines indicating the current path (calculated by a inversion method, see text) are superimposed on the grayscale image (more black corresponds to lower flux). Current profiles display $j_{c,L}$ and $j_{c,T}$ along the white dot-dashed lines marked by ○ and ▽ in the greyscale image.

whereas the magnitude remains the same. Thus, discontinuity lines divide the superconducting film into four domains with uniform current flow.

In homogeneous samples, the penetration depths of the flux fronts which start penetrating at the middle of different sample edges are the same.[32,33] With increasing external magnetic field, the penetration depth increases until the sample is completely filled by magnetic flux and the shielding current has reached the critical value j_c in the entire superconductor. As an example, Fig. 13 shows the calculated distribution of the magnetic flux at the surface of a 200 nm thick HTSC film of square shape (2 mm × 2 mm). An extension of the Bean model was used to calculate the flux pattern in the fully penetrated state.[32] The current lines superimposed on the grayscale image represent the critical current flowing parallel to the film borders. The density of these stream lines reflects the magnitude of the critical current density. The flux pattern shown in Fig. 13 is typical of *homogeneous* type-II superconductors, i.e., YBCO films grown on well-oriented $SrTiO_3$(001).

Figure 14 shows the magneto-optically observed flux pattern at the surface of a 360 nm thick YBCO film on $SrTiO_3$(106) in an external field $B_{ext}=32$ mT, at 4.2 K. The superimposed current lines were computed numerically from the measured flux density distribution by inversion of Biot-Savart's law (see following section). The dark spots in Fig. 14 result from defects in the iron garnet indicator film used as a field sensing element. Both, flux and current density distribution differ significantly from the usual behavior of homogeneous HTSC films (see Fig. 13 for comparison). The magnetic flux penetrates more easily in the L direction than in the T direction. Because the dependence of the penetration depth of the flux front on the external field is related to the critical current density, the anisotropic flux penetration in YBCO on $SrTiO_3$(106) also indicates an in-plane anisotropy of j_c. The anisotropic flux pinning results in two different critical current densities $j_{c,L}$ and $j_{c,T}$, parallel and perpendicular to the observed planar defect strucure, respectively.

The anisotropy ratio of the critical current density can be derived from the relation[32]

$$A_j=\frac{j_{c,T}}{j_{c,L}}=\frac{1}{\tan\alpha}, \tag{7}$$

where α is the angle between the discontinuity line and sample edge as visible in Fig. 14. Using Eq. (7), we find, respectively, $2\leqslant A_j(\theta=10°)\leqslant 5$ and $1.5\leqslant A_j(\theta=1.2°)\leqslant 2.5$ for YBCO films on $SrTiO_3$(106) and 1.2° miscut $SrTiO_3$(001) with different film thicknesses.

2. Systematics of the critical current density

By means of the MOFE we determine the z component (normal to the film surface) of the local magnetic induction $B_z(x,y)$ above the film surface. The magnetic induction results from a superposition of the external magnetic field $\mathbf{B_{ext}}=\mu_0\mathbf{H_{ext}}$ and a magnetic self-field $\mu_0\mathbf{H_{self}(r)}$, which is generated by the current density distribution $\mathbf{j(r)}$ in the sample according to Biot-Savart's law

$$\mu_0\mathbf{H_{self}}(\mathbf{r})=\frac{\mu_0}{4\pi}\int_{V'}\frac{\mathbf{j}(\mathbf{r}')\times(\mathbf{r}-\mathbf{r}')}{|\mathbf{r}-\mathbf{r}'|^3}\mathbf{d}^3\mathbf{r}'. \tag{8}$$

The current density distribution is directly computed from the measured $B_z(x,y)$ data using a numerical method to invert Eq. (8). In this way, we determine $j(x,y)$ with a lateral resolution of less than 10 μm. The computational method recently improved by Jooss *et al.* will be described in a separate publication.[34]

As an example, two profiles of the current density along the L and T directions in the 360 nm thick YBCO film on $SrTiO_3$(106) are shown in Fig. 14. We observe an enhanced

TABLE II. Summary of the critical current densities $j_{c,L}$ and $j_{c,T}$, as well as the anisotropy ratio $A_j = j_{c,L}/j_{c,T}$ at 30 mT and 4.2 K for YBCO films on $SrTiO_3(106)$ with different thicknesses t. The subscripts T and L indicate different crystallographic directions defined in the text.

Sample	t (nm)	$j_{c,L}$ 10^{11} A/m^2	$j_{c,T}$ 10^{11} A/m^2	A_j
A	22	5	1.5	3.3
B	55	8	1.7	4.6
C	240	8	3.0	2.7
D	360	2.5	0.8	3.1

critical current density $j_{c,L} = 2{,}5 \times 10^{11}$A/m^2, whereas $j_{c,T} = 0.8 \times 10^{11}$A/m^2 exhibits a magnitude generally observed in YBCO films.

We have studied the systematics of the flux penetration in YBCO films on $SrTiO_3(106)$ as a function of film thickness. Anisotropic flux pinning was observed for thicknesses ranging from 22 to 360 nm. Despite a large number of samples studied we cannot offer a conclusive picture of the dependence of j_c on thickness. The anisotropy ratio A_j and the critical current density j_c of some representative YBCO films on $SrTiO_3(106)$ with different thicknesses, determined at $B_{\text{ext}} \approx 30$ mT and 4.2 K, are summarized in Table II. However, A_j and j_c exhibit maximum values for thicknesses t between 50 and 250 nm, i.e., we observe $j_{c,L} = 8 \times 10^{11}$ A/m^2 and $A_j = 4.7$. Note that the critical current density $j_{c,L} = 8 \times 10^{11}$ A/m^2 exceeds by far the values generally observed in YBCO films. With $t > 250$ nm and $t < 50$ nm, the critical current density in the L direction is reduced, whereas $j_{c,T}$ remains almost constant.

In view of the evolution of the growth morphology described in the previous sections, it is reasonable to relate these findings to a thickness-dependent defect microstructure. However, variations of the perfection of the $SrTiO_3(106)$ substrate surface structure, some variations in the miscut as well as the patterning of the samples may result in deviations from a unique behavior. The thickness-dependent variation of the anisotropy ratio is predominantly caused by changes in $j_{c,L}$. It is associated with a macroscopic pinning force in the T direction which is in turn related to the defect planes (i.e., APB's) in the L direction. With a film thickness smaller than 50 nm, the terraces are frequently interrupted in the L direction (see Fig. 4), although they become continuous as growth proceeds. Moreover, the YBCO terraces become larger than those of the clean substrate, a fact which indicates that the number of APB's is somewhat reduced by a partial overgrowth of steps. Therefore, the maximum $j_{c,L}$ is observed if the microstructure in the L direction becomes homogeneous with a large density of APB's, i.e., if the defect microstructure exhibits a maximum anisotropy.

We find some ≈ 50 μm wide filamentary structures in the magnetic field distribution along the L direction for YBCO films on $SrTiO_3(106)$. The decreasing anisotropy ratio of the critical current density is associated with a smoothing and broadening of the filamentary structures with increasing film thickness. Further investigations of this phenomenon are in progress.

For $\theta = 1.2°$, the maximum critical current density is significantly smaller than that of YBCO films on $SrTiO_3(106)$, i.e., we observe $j_{c,L} \leqslant 2.2 \times 10^{11}$ A/m^2, and $j_{c,T}$ also ranges from $0.8 - 1.2 \times 10^{11}$ A/m^2. This finding suggests that the small APB's and stacking faults in films on $SrTiO_3(106)$ rather than the extended APB's in films on 1.2° miscut $SrTiO_3(001)$ are responsible for effective flux pinning.

B. Discussion of pinning mechanisms

In view of the fact that the exceptionally large critical current density $j_{c,L}$ is linked to anisotropic pinning forces, we restrict the discussion of possible pinning mechanisms to planar defects. In HTSC's effective pinning forces result from inhomogeneities on the length scale of ξ_{ab} ($\xi_{ab} << \lambda_{ab}$). We discuss in the following two sorts of pinning mechanisms usually called δT_c and δl ($\delta\kappa$) pinning[1] under the assumption that suprastrictive interactions (associated with stress fields near lattice defects) do not contribute significant pinning forces in HTSC's.[14] For δT_c pinning, disorder-induced spatial variations in T_c resulting from a local suppression of the superconducting order parameter ψ at defects predominantly cause a spatial modualtion of the linear and quadratic terms of the Ginzburg-Landau free-energy functional ($\alpha|\psi|^2 + \beta/2|\psi|^4$). In contrast, disorder-induced spatial variations of the charge carrier mean free path l, and possibly also the effective-mass tensor, near lattice defects that do not necessarily cause a significant suppression of ψ affect the nonlinear $|\nabla\psi|^2$ term leading to a different pinning mechanism, called δl pinning. To enable a *qualitative* understanding of the magnitude of j_c in YBCO films on $SrTiO_3(106)$, we provide a crude estimate of the pinning forces based on the observable experimental data.

1. Anisotropic δT_c pinning at planar defects

Because CuO_2 planes and CuO chains are partially broken across the APB's and we observe a spatially restricted distortion of the crystal lattice in conjunction with these defects, it is reasonable to assume a small local depression of the superconducting order parameter ψ associated with a local suppression of the transition temperature T_c at APB's. This assumption is sustained by the argument of Deutscher and Müller,[35] that the suppression of ψ at lattice defects is effected by the small coherence length $\xi_{ab}(4.2\text{ K}) \approx 1.5$ nm in YBCO. Generally, the relative suppression of T_c at defects is expressed in terms of a disorder parameter δ: $\delta T_c/T_c \approx \delta = 1 - |\psi_d/\psi_\infty|$, where ψ_d denotes the reduced order parameter at the lattice defect and ψ_∞ the order parameter associated with a homogeneous superconductor. To provide a quantitative estimate of the $\delta T_c/T_c$ at the observed APB's, we model the defect plane as a normal-superconducting interface with the resultant variation of the order parameter ψ given by[36] the linear extrapolation $d\psi/dx \approx \psi_\infty/b$. Using the expression[1] $b \approx \xi_{ab}^2/a$, where $a = 0.38$ nm is the mean in-plane lattice constant of YBCO, the extrapolation length b is found to be 5.9 nm. The disorder parameter δ characterizing a planar defect in a superconducting matrix can be estimated to be $\delta \approx r_p/2b$. With the structural width r_p of the APB's ranging between 0.7 and 2 nm as revealed by TEM, we obtain $\delta = 0.06$–0.17. Assuming $T_{c,0} = 90$ K, we thus find a T_c suppression of $\delta T_c = 5.4$–15.3 K at APB's.

For vortex interaction with a spatial variation of the transition temperature, expressed by the parameter δ, the pinning energy per unit length of a vortex that is pinned over a portion l_p/t of the film thickness is given by[1]

$$\epsilon_p = -\frac{l_p}{t}\frac{\delta\Phi_0^2}{4\pi\mu_0\lambda_{ab}^2}, \tag{9}$$

where Φ_0 is the flux quantum and λ_{ab} the penetration depth in the ab plane. The maximum pinning force which acts on a single vortex line in a direction perpendicular to the defect plane,

$$f_\perp \approx \epsilon_p/\xi_{ab} = \frac{\Phi_0^2}{4\pi\mu_0\lambda_{ab}^2}\frac{\delta l_p}{t\xi_{ab}}, \tag{10}$$

is related to the critical current density in the L direction. For small magnetic fields, we estimate

$$j_{c,L} \leqslant f_\perp/\Phi_0. \tag{11}$$

Assuming that $\delta T_c = 10$ K at an antiphase boundary and a maximum pinning length $l_p/t = 1$, we obtain $j_{c,L}^{\max} \approx 4\times10^{11}$ A/m^2 as an upper estimate of the critical current density. If, in fact, the relevant pinning length were $l_p/t < 1$, the T_c suppression at APB's would be significantly larger than 20 K in order to account for the observed exceptionally large critical current density $j_{c,L} \approx 8\times10^{11}$A/m^2. In view of the relatively large extrapolation length, and the fact that the structural width of most APB's is smaller than 1 nm, $\delta T_c > 20$ K appears to be unreasonable. However, such a strong T_c suppression may occur at the observed extended defects.

We observe the same magnitude of $j_{c,L}^{\max}$ if we take into account the fact that a vortex located at a planar defect with reduced T_c turns into a vortex with a highly anisotropic core,[37] i.e., Abrikosov-Josephson vortices are formed. These findings suggest that δT_c pinning at planar defects cannot explain the observed magnitude of $j_{c,L}$. An additional pinning mechanism is required which will be discussed in the following section.

2. Anisotropic δl pinning at planar defects

Pinning can also result from spatial variations δl in the charge-carrier mean free path l near lattice defects. As already shown by Zerweck,[38] carrier scattering at grain boundaries leads to pinning because of the spatially varying coherence length. It follows from the microscopic theory[39] that the pinning energy at a planar defect, which exhibits a structural width of $r_p \leqslant \xi_{ab}$ is enhanced by a factor $\xi_{ab}/r_p > 1$ in comparison with the predictions from Ginzburg-Landau theory. In fact, the existence of locations with enhanced carrier scattering helps the order parameter to adjust itself to the rapid changes required by the presence of the vortex with a normal conducting core. Recently, Griessen *et al.*[13] concluded from measurements of the temperature dependence of the critical current density that δl pinning is dominant in YBCO thin films.

In the following we provide an estimate of the critical current density for δl pinning at planar defects using quasiclassical theory, following the approach of Thuneberg.[40,14] The relevant quantities for the pinning energy can be expressed in terms of the charge-carrier mean free path l, which we compute from our experimental resistivity data of YBCO films on $SrTiO_3$(106). Because the observation of flux penetration into superconducting films by means of the MOFE is performed at low temperatures, we are interested in the mean free path l due to scattering by static disorder (lattice defects), characterized by the residual resistivity. In the static limit of the Drude model, l is related to the residual resistivity by

$$l = \frac{\hbar}{e^2}\left(\frac{3\pi^2}{n^2}\right)^{1/3}\frac{1}{\rho_0}, \tag{12}$$

where n is the hole density. As an example, we calculate l for the 60 nm thick film. Using a typical value of $n \approx 2.5\times10^{21}\mathrm{cm}^{-3}$ and the measured resistivity $\rho_{0,L} = 10\ \mu\Omega$ cm which is close to that observed in single crystals of YBCO, we find $l_L \approx 70$ nm in the L direction. The mean free path in the T direction can be estimated using $l_T \approx l_L\rho_{0,L}/\rho_{0,T}$ to be ≈ 2 nm. The smallness of l_T is reasonable, since according to our investigations of the structural properties of the YBCO films the growth-related APB's are typically 4–7 nm spaced apart. Consequently, the APB's with a structural width of $r_p < \xi_{ab}$ are very effective in sustaining the generation of large gradients in the order parameter which exist in the vicinity of a vortex core.

We use next a result from quasiclassical theory, developed from the BCS-Gor'kov theory, with the effect of planar defects modeled as scattering by numerous ($n\to\infty$) point defects which form a plane with $r_p < \xi_{ab}$. In this model, the pinning energy per unit length for small magnetic fields and high Ginzburg-Landau parameter κ is given by

$$\epsilon_p = \frac{8}{8.414\chi(\rho_i)}\left[\sum_{n=0}^{\infty}\frac{1}{(2n+1)^2(2n+1+\rho_i)^2}\right] \times\frac{H_c^2}{8\pi}S(p_{\mathrm{tr}\perp}+p_{\mathrm{tr}\parallel})U(x), \tag{13}$$

where H_c is the thermodynamical critical field, $\chi(\rho_i) \approx 0.95\Sigma_{n=0}^{\infty}[(2n+1)^2(2n+1+\rho_i)]^{-1}$ is the Gor'kov impurity function and $\rho_i \approx \xi_{ab}/l$ the impurity parameter. Because of the small mean free path $l_T \approx 2$ nm *perpendicular* ($\perp$) to the defect planes, it is reasonable to assume a transport scattering probability $p_{\mathrm{tr}\perp}$ to be in the order of $p_{\mathrm{tr}\perp} \approx 1$. To estimate the transport scattering probability $p_{\mathrm{tr},\parallel}$ *parallel* to the defect planes, we distinguish two cases: If a vortex is located between defect planes, $p_{\mathrm{tr},\parallel}$ is very small because $l_\parallel \approx 70$ nm resembles the value typically observed in single crystals. In contrast, if the vortex is directly located at a defect plane, we expect $p_{\mathrm{tr},\parallel} \approx 1$ because of the smallness of the mean free path $l_\perp \approx 2$ nm. Due to the defect-related anisotropy of the transport properties, the cross section S of the vortex core can be reasonably approximated by an elliptical area: $S = \pi\xi_\parallel\xi_\perp$. In Eq. (13), all factors of order of unity are neglected. In order to obtain the maximum pinning force we

use an upper estimate[14] of the pinning potential $U(x)$ which depends on the distance x between the vortex and the defect plane: $U(x) \approx 1.5$ (corresponding to a vortex sitting at the defect plane). Moreover, assuming $S \approx \pi \xi_{ab}^2$, we can derive $f_\perp$ from Eq. (13) and, thus, obtain $j_{c,L} = 1 \times 10^{12}$ A/m^2, neglecting the contribution of $p_{\mathrm{tr},\parallel}$ and using $l_p/t = 1$. For this estimate a mean free path $l = 2$ nm in the T direction was inserted in Eq. (13). If we consider additionally the parallel scattering for a vortex sitting in the APB plane, we obtain critical current densities of the same magnitude even if we assume a finite pinning length $l_p/t \approx 0.5$.

Our above calculations are based on gross estimates to enable a basic understanding of the exceptionally large critical current densties and therefore a connection to the observable experimental data. For a more quantitative treatment, the variation of the carrier mean free path in a network of planar defects must be modeled as a function of the distance and angle to a plane. Also, the change in coherence length with the mean free path and the formation of an elliptic vortex core at the scattering plane[38] must be taken into account.

Experimental measurements indicate a different dependence of $j_{c,L}$ and $j_{c,T}$ on temperature and magnetic field. Further studies to establish a conclusive picture of the dominant pinning mechanism in these particular films are in progress.

VI. CONCLUSION

We have generated substrate surfaces, ideally suited to introduce an array of antiphase boundaries with determined density into epitaxial YBCO films. The vicinal surface $SrTiO_3(106)$ promotes self-organization of the YBCO adlayer in a particularly efficient way. The resultant microstructure, aligned with the regular substrate step edges, leads to a pronounced thickness-dependent anisotropy of the in-plane resistivity and flux penetration into samples of square shape. Specifically, we find an exceptionally large critical current density up to 8×10^{11} A/m^2. Connecting the experimental observations with microscopic pinning theories indicates that δl pinning, related to an array of antiphase boundaries and stacking faults, is responsible for this strong enhancement of j_c. This presented results suggest that the film growth on tailored substrate surfaces is a promising tool in scientific investigations of pinning mechanisms and technologically driven efforts to enhance the critical current density in HTSC's and to tailor anisotropic transport properties.

ACKNOWLEDGMENTS

This work was supported partially by the German BMBF Contract No. 13N5840 and the European Union Contracts No. EU CHRX-CT 94-0523 and EU CHRX-CT 930137.

[1] G. Blatter, M. V. Feigel'man, V. B. Geshenbein, A. I. Larkin, and V. M. Vinokur, Rev. Mod. Phys. **66**(4), 1125 (1994).
[2] H. Theuss and H. Kronmüller, Physica C **177**, 253 (1991).
[3] M. Oussena, P. A. J. de Groot, S. J. Porter, R. Gagnon, and L. Taillefer, Phys. Rev. B **51**, 1389 (1995).
[4] L. Civale, A. D. Marwick, T. K. Worthington, M. A. Kirk, J. R. Thompson, L. Krusin-Elbaum, J. R. Clem, and F. Holtzberg, Phys. Rev. Lett. **67**, 648 (1991).
[5] Th. Schuster, H. Kuhn, M. V. Indenbom, G. Kreiselmeyer, M. Leghissa, and S. Klaumünzer, Phys. Rev. B **53**, 2257 (1996).
[6] D. S. Misra, B. D. Padalia, S. P. Pai, R. Pinto, and S. B. Palmer, Thin Solid Films **245**, 186 (1994).
[7] O. Eibl and B. Roas, J. Mater. Res. **5**, 2620 (1990).
[8] S. Senoussi, K. Frikach, and C. Colliex, Physica C **235-240**, 2767 (1994).
[9] H. Kronmuüller, Ch. Jooss, A. Forkl, R. Warthmann, H.-U. Habermeier, and B. Leibold, Physica C **266**, 235 (1996).
[10] H. W. Weber, R. M. Schalk, K. Kundzins, E. Stangl, S. Proyer, and D. Bäuerle, Physica C **257**, 341 (1996).
[11] J. Mannhart, D. Anselmetti, J. G. Bednorz, A. Catana, Ch. Gerber, K. A. Müller, and D. G. Schlom, Z. Phys. B **86**, 177 (1992).
[12] D. H. Lowndes, D. K. Christen, C. E. Klabunde, Z. L. Wang, D. M. Kroeger, J. D. Budai, Shen Zhu, and D. P. Norton, Phys. Rev. Lett. **74**, 2355 (1995).
[13] R. Griessen, Wen Hai-hu, A. J. J. van Dalen, B. Dam, J. Rector, H. G. Schnack, S. Libbrecht, E. Osquiguil, and Y. Bruynseraede, Phys. Rev. Lett. **72**, 1910 (1994).
[14] E. V. Thuneberg, Cryogenics **29**, 236 (1989).
[15] X-ray diffraction measurements reveal that YBCO films on $SrTiO_3(106)$ exhibit a preferrential orientation of the *b* axis along the step edges; J. Brötz *et al.* (unpublished).
[16] H.-U. Habermeier and H. Kronmüller, Appl. Phys. **12**, 297 (1977).
[17] A. A. Chernov, in *Modern Crystallography*, edited by H. J. Queisser (Springer, Berlin, 1984), Vol. 3, pp. 64–70.
[18] T. Haage, J. Zegenhagen, and M. Cardona (unpublished).
[19] Q. D. Jiang and J. Zegenhagen, Surf. Sci. **338**, L882 (1995).
[20] Q. D. Jiang and J. Zegenhagen, Surf. Sci. **367**, L42 (1996).
[21] T. Haage, H.-U. Habermeier, and J. Zegenhagen, Surf. Sci. **370**, L158 (1997).
[22] We estimate the volume fraction of Y_2O_3 in our films to be smaller than 1%. In particular, this off-stoichiometric material cannot be detected by x-ray diffraction.
[23] J. Zegenhagen, T. Siegrist, J. R. Patel, E. Fontes, and L. E. Berman, Solid State Commun. **93**, 763 (1995).
[24] H. F. Poulsen, N. H. Andersen, J. V. Andersen, H. Bohr, and O. G. Mouritsen, Nature (London) (London) **349**, 594 (1991).
[25] V. Hadjev (private communication).
[26] A. A. Abrikosov and L. P. Gorkov, Sov. Phys. JETP **12**, 1243 (1961); A. A. Abrikosov, Physica C **214**, 107 (1993).
[27] G. Deutscher and P.G. de Gennes, in *Superconductivity*, edited by R. D. Parks (Marcel Dekker, New York, 1969), pp. 1008–1009.
[28] T. A. Friedmann, M. W. Rabin, J. Giapintzakis, J. P. Rice, and D. M. Ginsberg, Phys. Rev. B **42**, 6217 (1990).
[29] A. G. Rojo and K. Levin, Phys. Rev. B **48**, 16 861 (1993); A. A. Abrikosov, *ibid.* **52**, R7026 (1995).
[30] J. Halbritter, M. R. Dietrich, H. Küpfer, B. Runtsch, and H. Wühl, Z. Phys. B **71**, 411 (1988).
[31] T. R. Lemberger, in *Physical Properties of High Temperature Superconductors III*, edited by D. M. Ginsberg (World Scientific, Singapore, 1992) pp. 474–479.
[32] A. Forkl and H. Kronmüller, Phys. Rev. B **52**, 16 130 (1995).
[33] Th. Schuster, H. Kuhn, E. H. Brandt, M. V. Indenbom, M. Kläser,

G. Müller-Vogt, H.-U. Habermeier, H. Kronmüller, and A. Forkl, Phys. Rev. B **52**, 10 375 (1995).
[34] Ch. Jooss, R. Warthmann, A. Forkl and H. Kronmüller (unpublished).
[35] G. Deutscher and K. A. Müller, Phys. Rev. Lett. **59**, 1745 (1987).
[36] P. G. De Gennes, Rev. Mod. Phys. **36**, 225 (1964).
[37] A. Gurevich and L. D. Cooley, Phys. Rev. B **50**, 13 563 (1994).
[38] G. Zerweck, J. Low Temp. Phys. **42**, 1 (1981).
[39] E. V. Thuneberg , J. Kurkijärvi, and D. Rainer, Phys. Rev. Lett. **48**, 1853 (1982).
[40] E. V. Thuneberg , J. Low Temp. Phys. **62**, 27 (1986).